Detailed XMM-Newton Observation of the Cluster of Galaxies Abell 1060

Akira HAYAKAWA[1], Akio HOSHINO[1], Manabu ISHIDA[1], Tae FURUSHO[2], Noriko Y. YAMASAKI[2], and Takaya OHASHI[1]

[1] *Department of Physics, Tokyo Metropolitan University, 1-1 Minami-Osawa, Hachioji, Tokyo 192-0397*

[2] *Institute of Space and Astronautical Science, Japan Aerospace Exploration Agency, 3-1-1 Yoshinodai, Sagamihara, Kanagawa 229-8510*

E-mail(MI): ishida@phys.metro-uac.jp

(Received 2000 December 31; accepted 2001 January 1)

Abstract

We present results from the *XMM-Newton* observation of the non-cooling flow cluster A 1060. Large effective area of *XMM-Newton* enables us to investigate the nature of this cluster in unprecedented detail. From the observed surface brightness distribution, we have found that the gravitational mass distribution is well described by the NFW profile but with a central density slope of $\sim$1.5. We have undoubtedly detected a radial temperature decrease of as large as $\sim$30% from the center to the outer region ($r \sim 13'$), which seems much larger than that expected from the temperature profile averaged over nearby clusters. We have established that the temperature of the region $\sim 7'$ southeast of the center is higher than the azimuthally averaged temperature of the same radius by $\sim$20%. Since the pressure of this region already reaches equilibrium with the environment, the temperature structure can be interpreted as having been produced between 4×10^7 yr (the sound-crossing time) and 3×10^8 yr (the thermal conduction time) ago. We have found that the high-metallicity blob located at $\sim 1\farcm5$ northeast of NGC 3311 is more extended and its iron mass of 1.9×10^7 $M_\odot$ is larger by an order of magnitude than estimated from our *Chandra* observation. The amount of iron can still be considered as being injected solely from the elliptical galaxy NGC 3311.

Key words: galaxies: clusters: individual (Abell 1060) – galaxies: intergalactic medium – X-ray: galaxies

1. Introduction

Clusters of galaxies, being the largest virialized systems in the universe, are filled with the intracluster medium(ICM), which consists of X-ray emitting hot plasma with a typical temperature of a few $\times 10^7$ K. The ICM gives us rich information about the structure and evolution of clusters of galaxies. X-ray Spectra of ICM immediately reveal its temperature and metal abundance, and the ICM surface brightness shows us ICM density distribution. Through the assumption of hydrostatic equilibrium, furthermore, it is possible to measure the distribution of the gravitational mass in clusters.

The cluster mass distribution is an important observational clue in determining the nature of the dark matter and in constraining the structure formation scenario. In particular, the CDM model predicts a significant central cusp in the dark matter profile

(Navarro, Frenk, & White 1996), in contrast to the flat core profile described by the β model. High-sensitivity X-ray study is a powerful method to look into the gravitational mass distribution (e.g. Churazov et al. 2003). For clusters characterized by cool central cores, presence of the bright central galaxy greatly hampers the mass determination for the pure cluster component. Therefore, detailed study of a non cool-core cluster has a significant importance.

Recent observational studies of the clusters with *Chandra* and *XMM-Newton*, with their powerful imaging capability and large effective area, unveiled a lot of new interesting features. Mazzotta et al. (2003) found an unusual X-ray morphology, blob and hole like features, in the central dense region of the 2A 0335+096 cluster. Markevitch et al. (2000) detected sharp brightness edges, called cold fronts, with lower temperature inside the subcluster in A 2142 cluster. Furusho et al. (2003) found two high-metallicity blobs located symmetrically with respect to the center of the poor cluster AWM 7. Piffaretti et al. (2005) investigated temperature profiles of 13 nearby cooling flow clusters observed with *XMM-Newton*, and found that the temperature decreases by $\sim$30% between 0.1 r_{vir} and 0.5 r_{vir}. This feature is in good agreement with the result of Markevitch et al. (1998) who found that the temperature of 30 nearby clusters show a significant decline at large radii. Recent *Chandra* observation of A 1060 revealed that the central two elliptical galaxies emit X-ray (Yamasaki et al. 2002), and the temperature and the abundance distribution are unexpectedly inhomogeneous (Hayakawa et al. 2004).

A 1060 is a nearby cluster ($z = 0.0114$) characterized by a smooth and symmetric ICM distribution. The ASCA and ROSAT observations found that the temperature and the abundance showed very uniform distribution (Tamura et al. 1996; Furusho et al. 2001). For these reasons, this cluster was thought to be in a highly relaxed state, and has been used to estimate the gravitational mass profile which can be directly compared with the results of hydrodynamic cluster simulation (Tamura et al. 2000).

In this paper, we report the results of *XMM-Newton* observation of the A 1060 cluster. Based on the surface brightness distribution, we have computed the total gravitational mass of

the cluster. We confirmed the existence of the high-metallicity blob discovered by our *Chandra* observation but with a larger iron mass content. Using the high spatial resolution and the large effective area, we searched for a sign of a sub-cluster merger from a two-dimensional temperature map. Throughout this paper, we assume $H_0 = 75$km s^{-1} Mpc^{-1} with $q_0 = 0.5$. Accordingly, an angular size of $1'$ corresponds to 13 kpc. The solar number abundance of iron relative to H is assumed to be 4.68×10^{-5} (Anders & Grevesse 1989). We employ Galactic absorption as $N_{\rm H} = 4.9 \times 10^{20}$cm^{-2}.

2. Observation and Data reduction

The *XMM-Newton* observation of the A 1060 cluster of galaxies was carried out on 2004 June 29 for a total exposure time of 64 ksec. All the EPIC cameras were operated in the Full frame mode with the medium filter inserted. Data reduction and analysis were performed with SAS version 6.0 and CIAO 3.0. Unfortunately, part of the data was affected by high background flares. In order to remove them, we adopted the following data cleaning process. We made light curves in the bands 10-12 keV for MOS and 12-14 keV for pn, where the signals are dominated by background events, and then we removed the time interval when the count rate is larger than 0.3 c s^{-1} for MOS and 0.8 c s^{-1} for pn. Then, we selected the photon events with pattern 0-12 for MOS and 0-4 for pn, and flag=0 [1] . After these selections, some 35.9, 36.4, and 25.2 ksec of good time intervals remained for MOS1, MOS2, and pn, respectively.

The blank sky data sets of Read & Ponman (2003) were used to subtract the background of our data sets. We extracted the background events using the same selection criteria as above. The source-to-background count-rate ratio was calculated from the count rates in the bands 10-12 and 12-14 keV for MOS and pn (see Katayama et al. 2004), which result in 1.132, 1.250, and 1.200 for MOS1, MOS2, and pn, respectively. After subtracting the blank sky data, being scaled by these factors, from the source data sets, we created X-ray images for each detector separately. Figure 1 (a) and (b) show the X-ray image of MOS1 in the band 0.8-8.0 keV. The telescope vignetting effect had been corrected using the exposure map which was calculated with the SAS "eexpmap" [2] command. The image had been smoothed by a Gaussian with a 1σ width of $4.4''$ using the CIAO csmooth command. The two bright elliptical galaxies (NGC 3311 and NGC 3309) are clearly visible in the central region of the cluster (Fig. 1 (b)). Properties of these galaxies have been reported by Yamasaki et al. (2002). A blob-like high brightness region was located at northeast of NGC 3311. Except for these central features, the whole surface brightness distribution remains nearly spherically symmetric. Although the surface brightness map in Fig. 1(a) seems elongated in the north-south direction, the lengths of the semi-major/minor axes of the isophote at $r \simeq 5'$, for example, agree within a few percents.

[1] http://xmm.vilspa.esa.es/sas/current/doc/evselect/

[2] http://xmm.vilspa.esa.es/sas/current/doc/eexpmap/

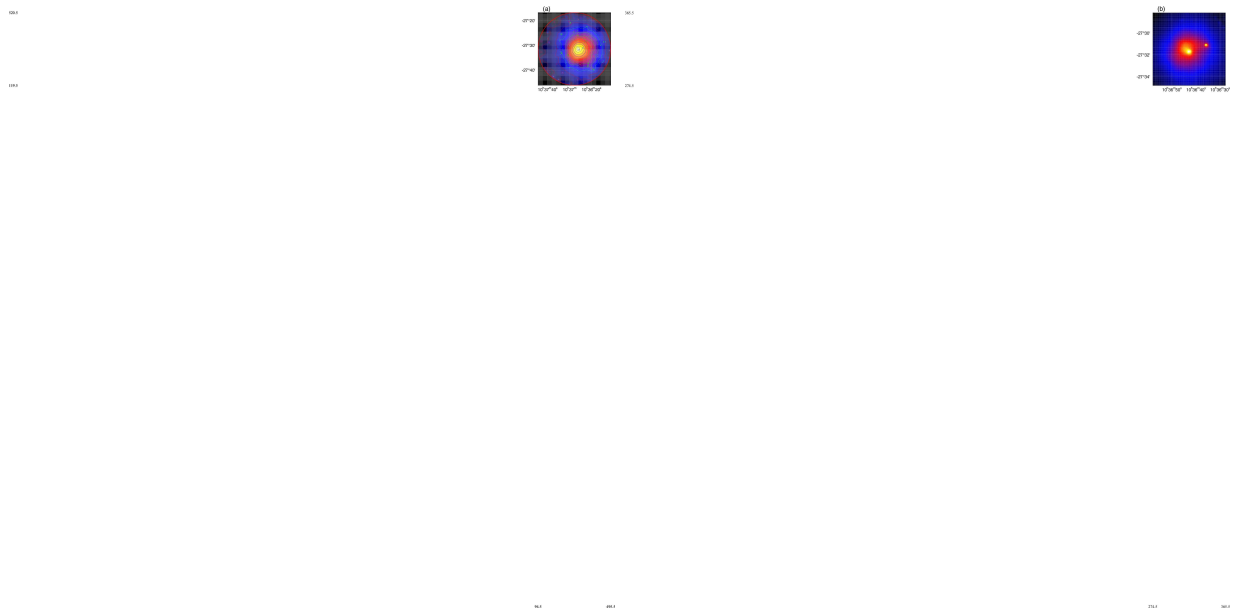

Fig. 1. (a) Adaptively smoothed MOS1 X-ray image of the $30' \times 30'$ region, overlaid with the intensity contours. The contours were logarithmically scaled and divided into 20 spaces between 10^{-5} and 10^{-3}counts s^{-1} range. The red circle represents *XMM-Newton* field of view. (b) Close up view in the central $8' \times 8'$ region.

We created on-source spectra of each detector within a radius of $13'$ from the cluster center. The point-like sources seen in Fig. 1 were removed using SAS "edetect_chain" [3] command. The central two elliptical galaxies possess an extended halo (Yamasaki et al. 2002). Accordingly, we have excluded manually the circular regions with radii of $25''$ and $20''$ centered on NGC 3311 and NGC 3309, respectively, for accumulating spectra in order to avoid contamination from the halo. The blank sky spectra were subtracted from the on-source spectra after the appropriate scalings to remove the background photons. For pn data, there are strong fluorescence lines of Ni, Cu and Zn at around 8 keV. Since these lines can not be completely removed by the background subtraction, we introduce Gaussians in the spectral model to represent these lines. First of all, we fitted the spectra from each detector separately with the absorbed MEKAL model in the bands 0.8-8.0 keV for MOS1,2 and 0.8-10.0 keV for pn. As summarized in table 1, with the absorption fixed at the galactic value of $N_{\rm H} = 4.9 \times 10^{20}$ cm^{-2} (Dickey & Lockman 1990), the temperature is distributed in the range 3.10-3.30 keV among the three detectors. If the $N_{\rm H}$ value is set free to vary, a similar temperature distribution (kT = 3.13-3.31 keV) is obtained. The $N_{\rm H}$ value from the pn fit, however, shifted to a lower value of $1.2^{+0.5}_{-0.4} \times 10^{20}$ cm^{-2}, which is significantly smaller than 4.9×10^{20} cm^{-2} obtained from the radio 21 cm measurement (Dickey & Lockman 1990). We then carried out a combined fit of the absorbed MEKAL model to the MOS1+2 and pn spectra of the $r < 13'$ region in the band 2.0-10.0 keV, free from the

[3] http://xmm.vilspa.esa.es/sas/current/doc/edetect_chain/

Table 1. Best-fit Parameters of the MEKAL model to the Spectra in the central $r < 13'$ region

Inst.	kT [keV]	Z [$Z_\odot$]	N_H [$\times 10^{20}$ cm^{-2}]	χ^2/d.o.f
MOS1	$3.30^{+0.04}_{-0.04}$	$0.41^{+0.02}_{-0.02}$	4.9(fix)	1.244
	$3.23^{+0.05}_{-0.05}$	$0.40^{+0.02}_{-0.02}$	$6.0^{+0.6}_{-0.6}$	1.226
MOS2	$3.20^{+0.03}_{-0.04}$	$0.41^{+0.02}_{-0.02}$	4.9(fix)	1.366
	$3.13^{+0.05}_{-0.05}$	$0.40^{+0.02}_{-0.02}$	$6.1^{+0.6}_{-0.6}$	1.344
pn	$3.10^{+0.03}_{-0.02}$	$0.37^{+0.01}_{-0.01}$	4.9(fix)	1.475
	$3.31^{+0.02}_{-0.02}$	$0.39^{+0.02}_{-0.02}$	$1.2^{+0.5}_{-0.4}$	1.238
MOS+pn				
> 2 keV	$3.39^{+0.04}_{-0.04}$	$0.35^{+0.02}_{-0.02}$	4.9(fix)	1.145
> 0.8 keV[a]	$3.27^{+0.02}_{-0.02}$	$0.39^{+0.02}_{-0.01}$	4.9(fix)	1.250

NOTE — All errors are at the 90% confidence level.

a: The energy bands for MOS and pn are 0.8-8 keV and 1.6-10 keV, respectively.

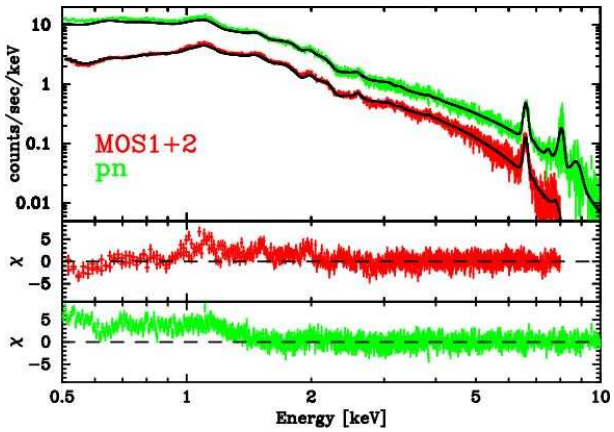

Fig. 2. MOS1+2 and pn spectra extracted from the r$< 13'$ region fitted in the bands 0.5-8 keV and 0.5-10 keV, respectively, with the MEKAL model undergoing the galactic absorption.

absorption, and simply retrieved the data points below 2 keV. The result is shown in Fig. 2. The hydrogen column density is fixed at the galactic value, 4.9×10^{20} cm^{-2}. The best-fit parameters are summarized in table 1. The MOS and pn results are inconsistent below $\sim$1 keV, and the pn fit requires a strong soft excess. A similar phenomenon has been reported from the *XMM-Newton* observation of A 1413 (Pratt & Arnaud 2002). According to these authors, this effect could be due to a true soft excess emission (e.g. Durret et al. 2002) and/or an artifact due to remaining calibration uncertainties. In the case of A1060, however, such a soft excess is incompatible with previous observations (Tamura et al. 2000). Accordingly, we neglect the energy band below 1.6 keV for the pn, and hereafter adopt the 0.8-8.0 keV and 1.6-10.0 keV

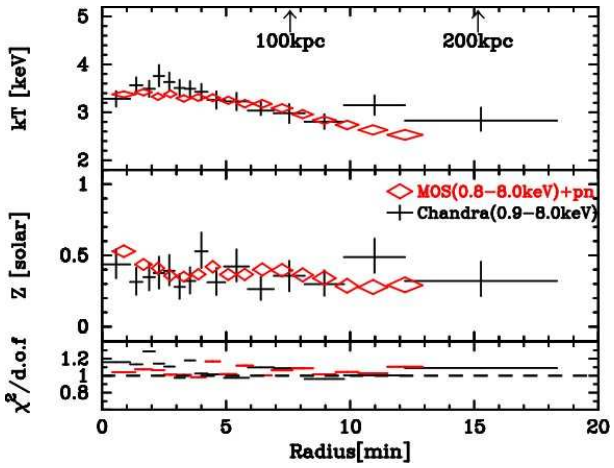

Fig. 3. Radial distributions of the temperature (top), metal abundance (middle), and reduced χ^2 value (bottom) of the spectral fits to the concentric annular regions. The red diamonds show the results from the MOS spectra in the bands 0.8-8.0 keV (pn energy band is fixed in 0.8-8.0 keV). The black dots show the result of *Chandra* observation. The error bars are at the single-parameter 90% confidence level.

bands for the MOS and the pn, respectively. The results of the combined fit in these energy bands are also summarized in table 1, showing that the temperature of the plasma within the projected central $r < 13'$ region is 3.27±0.02 keV with the metal abundance of $0.39^{+0.02}_{-0.01} Z_\odot$.

3. Temperature and Abundance Distribution

3.1. Radial Profile

We have produced radial temperature and abundance profiles in annuli centered on the position of NGC 3311. The central two elliptical galaxies (NGC 3311, NGC 3309) and the other point-like sources are removed (§ 2). The annuli are segmented from inner to outer radii so that they include at least 20,000 photons for all the detectors. The resulting widths of the annuli are ∼30″ or larger, which is larger than the HPD of the XRT (∼17″). The MOS and pn spectra in the bands 0.8-8.0 keV and 1.6-10.0 keV, respectively, are fitted simultaneously with an absorbed MEKAL model. The absorber's hydrogen column density is fixed at the Galactic value of 4.9×10^{20} cm^{-2}. Figure 3 shows the result of radial temperature and abundance distributions. For comparison, we have overlaid the *Chandra* results (Hayakawa et al. 2004). Owing to large effective area of *XMM*, the gradual temperature decline from $kT = 3.5$ keV to 2.5 keV toward the outer radii, which is not very clear in the *Chandra* result, is unambiguously detected. Because the field of view of the *Chandra* observation was offset toward the southwest direction, the outer two annuli were of poor statistics and probably affected by background uncertainty. The radial abundance increase of ∼20 % in the inner 3′ region also becomes very clear for the first time.

We have so far adopted the position of NGC 3311 as the cluster center simply because

it locates at the apparent peak of the surface brightness, and one may suspect that the radial profiles shown in Fig. 3 could be significantly different if we draw them centered on a different position. Accordingly, as an alternative, we have tried to define a cluster center with the geometry of the isophotes. We have fitted a circle to every isophote shown in Fig. 1(a) with its central position and radius being set free to vary, and have found that the center of the circle fitted to the second largest isophote ($r \sim 11'$) shows the largest shift of $22''$ from NGC 3311 in the western direction. We have made the radial profiles again with this new center. The resultant difference from the previous results is, however, quite small, which is only 5% and 15% at most for the temperature and the abundance over the entire radius range, respectively. In particular, the 5% random difference in the temperature is much smaller than the systematic temperature drop from 3.5 keV at the center to 2.5 keV at $r = 13'$. Accordingly, we adopt the position of the galaxy NGC 3311 as the cluster center throughout this paper.

3.2. Two-Dimensional Distribution

3.2.1. Temperature distribution

By taking full advantage of large effective area of *XMM-Newton*, we have attempted to draw a two-dimensional temperature map on the basis of spectral analysis. We divided each annulus which was adopted to obtain the radial profiles in Fig. 3 evenly into 8 azimuthal sectors. The radial width of annuli was determined by requiring a minimum of 8000 counts for all the eight sectors. The spectra were fitted, after background subtraction, with a single-temperature MEKAL model with the galactic absorption. This process is the same as that described in 3.1. Figure 4(a) and (b) show the resulting two-dimensional temperature distribution, and its radial profiles in the eight azimuthal directions, respectively. For reference, the azimuthally-averaged radial temperature profile (Fig.3) is overlaid in panel (b). It is remarkable that the $r = 4'-8'$ region in the two south-eastern sectors (labelled SE and ES in the figure) seems to be hotter than the other sectors at the same radii.

3.2.2. Metal distribution

We reported several high-metallicity regions near the center of A 1060 cluster ($r < 5'$) based on our *Chandra* observation (Hayakawa et al. 2004). We thus attempted to produce fully two-dimensional metal abundance map in the central $r \lesssim 4'$ region. We divided the sky region into rectangular cells with $22''$ on a side, and evaluated the metal abundance by fitting MEKAL model to the spectra obtained from 3×3 cells. We have obtained two-dimensional metallicity distribution through taking running average by shifting the integration region stepped by one cell. In order to keep statistical quality, we discard any 3×3 cell if it does not contain at least 4000 counts. The result is shown in Figure 5(a). A typical statistical error of the metallicity is 10–15%. We note that there is clearly a high-metallicity region at $\sim 1\farcm5$ northeast of NGC 3311 whose position is consistent with the blob detected with the *Chandra* observation. The projected metallicity within a radius of $1'$ centered on the blob is $0.65 \pm 0.06 Z_{\odot}$, which is compatible with

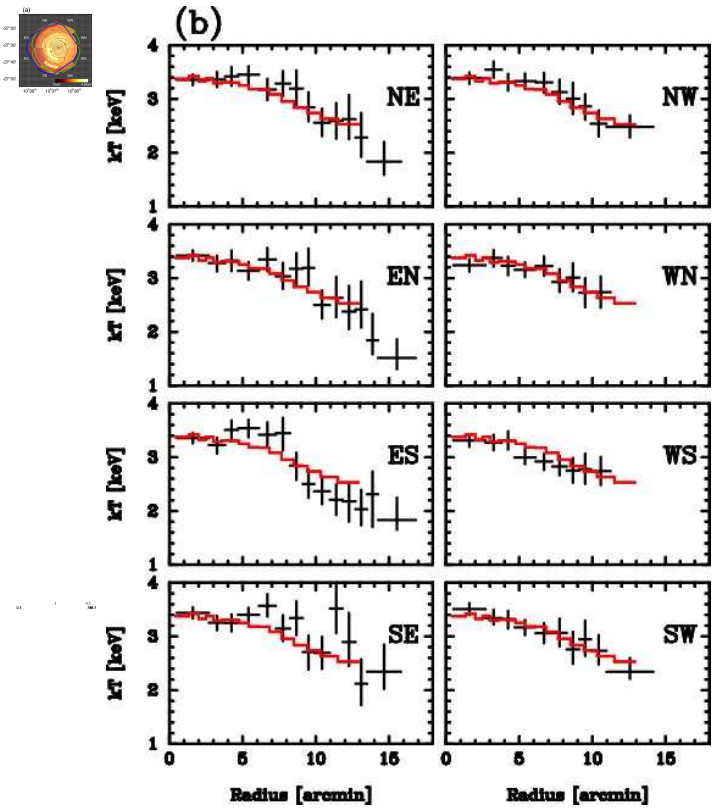

Fig. 4. (a):Temperature map obtained from spectral fits. The overlaid contours show smoothed X-ray surface brightness. The three lines indicate MOS1(red), MOS2(green), and pn(blue) fields of view. (b):Radial temperature profiles of the 8 sectors shown in (a). The red line shows the azimuthally-averaged radial temperature profile shown in Fig.3 (top panel), ignoring errors.

the *Chandra* value of $0.74^{+0.29}_{-0.23}Z_{\odot}$, and is about twice as large as in other regions. Figure 5(b) shows a radial metallicity distribution in the concentric annuli centered on the blob. Assuming that the metallicity of the ICM out of the blob region is uniform at $\sim 0.4Z_{\odot}$, the deprojected central metallicity of the blob is obtained to be $\sim 1.5Z_{\odot}$, which is consistent with the *Chandra* value (Hayakawa et al. 2004). Note, however, that the radial extent of the high-metallicity region is found as large as $r \simeq 2'$ (Fig. 5b), whereas it was only $\sim 40''$ in the *Chandra* observation. This is because the brightness of the blob is low and close to the photon limit of the *Chandra* ACIS. None of the other high-metallicity blob-like regions suggested by the *Chandra* observation, which are all fainter than the central blob, was significantly detected in the *XMM-Newton* observation.

4. Discussion

The present *XMM-Newton* observation of A 1060 provided several pieces of new knowledge on the surface brightness, temperature and abundance distributions in unprecedented detail. They include the significant drop of the temperature toward outer radii (§ 3.1), the

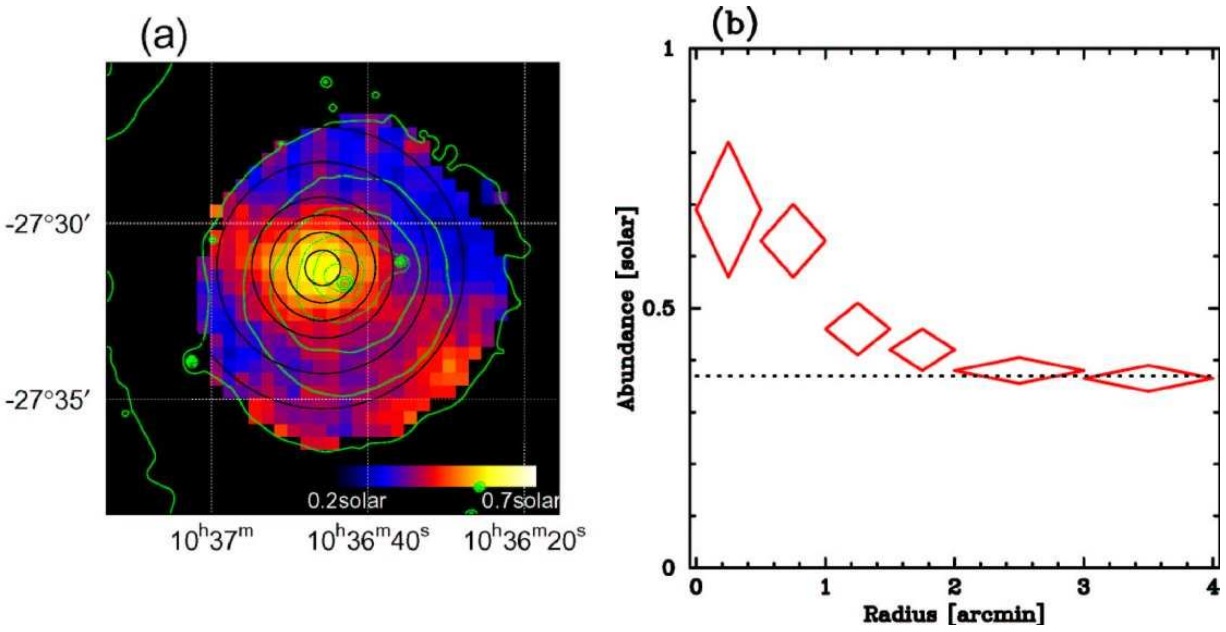

Fig. 5. (a) Metal abundance distribution in the central $r < 5'$ region based on spectral analysis. The pixel size is $22'' \times 22''$ (5kpc across). Spectral analysis is carried out for a square region of 3×3 pixels. The overlaid contours show smoothed X-ray surface brightness. (b) Radial metallicity distribution in annuli centered on the position of the high-metallicity blob, according to the concentric annuli of (a).

existence of the south-eastern high temperature region (§ 3.2.1), the high-metallicity blob in the central region (§ 3.2.2), and so on. We discuss their implication in some detail.

4.1. Mass Distribution

We first derive the gravitational mass profile based on the density distribution according to the following steps (see also § 4.2 of Hayakawa et al. 2004):

1. We first calculate the radial surface brightness profile from the MOS1+2 image in the 0.8-8.0 keV band, after application of the SAS task "evigweight" in order to eliminate the telescope vignetting effect.
2. Under the assumption of constant temperature and spherically symmetric distribution of the ICM, we fit the radial surface brightness profile in the range $r > 5'$ with a single β-model. The fitted parameters are $r_c = 7'.3 \pm 1'.8$ and $\beta = 0.69^{+0.11}_{-0.22}$, respectively.
3. The best-fit β-model is extrapolated to the center, and the ratio of the data to the model is calculated as a function of the radius. The radial profile of the surface brightness ratio is fitted with an exponential function.
4. The density of the plasma $\rho(r)$ predicted by the β-model is enhanced by multiplying the square root of the above ratio, and the new radial profile of the brightness is calculated.
5. The procedures 3 and 4 are repeated until the residual between the data and the model practically vanishes.

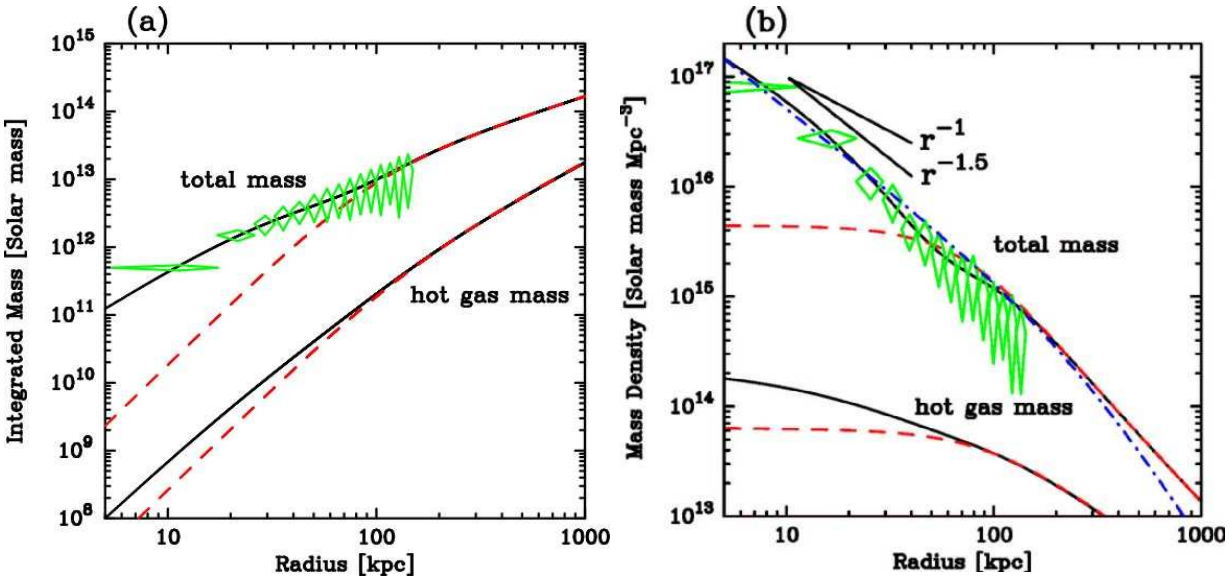

Fig. 6. (a) Gravitational mass profile estimated from the single β-model (upper dashed line) and the one obtained from our analysis (upper solid line) under the assumption of the isothermal ICM in hydrostatic equilibrium. The lower lines represent ICM masses only. The radial temperature gradient (Fig. 3) is reflected for the diamonds. (b) Gravitational mass density profile based on (a). The dashed-dotted line shows the Moore's model. Two representative slopes, $r^{-1.5}$ and r^{-1}, are also shown by solid lines.

As a result, we obtained the central electron number density to be $n_0 = 11.7^{+0.7}_{-0.6} \times 10^{-3}$ cm^{-3}. This value is slightly larger than that obtained from the *Chandra* observation $n_0 = 8.2^{+1.8}_{-1.0} \times 10^{-3}$ cm^{-3} (Hayakawa et al. 2004). This is mainly because we have substituted the exponential function for the Gaussian adopted for the *Chandra* data in the procedure 3 above. Since the statistics of the radial surface brightness profile of *Chandra* data was poor at the cluster center, the choice of the model to fit to the data-to-model ratio, especially at the cluster center, is not unique. We thus simply adopted the Gaussian with no particular reason. In analysing the high quality *XMM-Newton* data, however, we have found that the exponential function is significantly better than the Gaussian.

Given the radial density profile that can reproduce the surface brightness distribution, we then calculate the total gravitational mass with the equation

$$M_{tot}(< r) = -\frac{rkT(r)}{\mu m_p G}\left(\frac{d\ln\rho(r)}{d\ln r} + \frac{d\ln T(r)}{d\ln r}\right)$$

under to assumption of the hydrostatic equilibrium and the spherical symmetry of ICM. The integrated gravitational and gas mass profiles are shown by the solid lines in Fig. 6(a) under the assumption of the constant temperature $T(r) = \langle T \rangle$ (=3.3 keV; § 2). The corresponding mass density profiles are also shown in Fig. 6(b). For comparison, those assuming the single β-model are plotted with the red dashed lines. Shown by diamonds are the profiles that reflect the radial temperature variation (Fig. 3). Owing to large effective area of *XMM-Newton*, we

have unveiled the significant concentration of mass in the central region that can be represented by a density cusp with $\propto r^{-1.5}$. In order to confirm this, we tried a brief model fitting to the observed profile in Fig. 6(b). We tried two analytical models; the NFW model (Navarro, Frenk, & White 1997) and the Moore's model (Moore et al. 1999). They have a central density cusp proportional to r^{-1} and $r^{-1.5}$, respectively. As a result, we found that Moore's profile could be better fit to the data, which is displayed in Fig. 6(b) with the dash-dotted line. The central cusp of the gravitational mass density profile in A 1060 was first suggested by Tamura et al. (2000) based on the analysis of the *ASCA* and *ROSAT* data. Their analysis, however, did not take into account the compact halo associated with the elliptical galaxy NGC 3311 which could raise the cusp-like density enhancement. In the analysis of *Chandra* data, we could remove contribution from NGC 3311. Poor statistics, however, precluded us from detecting the density cusp of the total mass (Hayakawa et al. 2004).

The gravitational mass profile allows us to compute r_Δ for an overdensity Δ using

$$\Delta = \frac{3M_{tot}(< r_\Delta)}{4\pi\rho_c r_\Delta^3},$$

where ρ_c is the critical density (Piffaretti et al. 2005). In the SCDM model, the virial radius corresponds to $\Delta = 180$. Our total mass distribution indicates r_{180} to be about 1.35 Mpc. This is in good agreement with the theoretical prediction by Evrard, Metzler, & Navarro (1996), $r_{180} = 2.6$ Mpc $(T_X/10$ keV$)^{1/2}$, giving $r_{180} = 1.49$ Mpc for $T_X = \langle T \rangle = 3.3$ keV, as the mean emission-weighted temperature. We hereafter adopt $r_{180} = 1.35$ Mpc.

4.2. Abundance Distribution

The metal abundance distribution in the central $r < 5'$ region (Fig. 5) indicates a high-metallicity region centered at $\sim 1\farcm5$ northeast of NGC 3311. This enhancement was identified in our *Chandra* paper as the metal rich blob with a radius of $40''$ (= 8.7 kpc). We estimated the total mass of iron contained in the blob to be 3.0×10^6 $M_\odot$. *XMM-Newton* data showed, however, that the size of the high-metallicity region is significantly more extended than the *Chandra* result even considering an image blur of the *XMM-Newton* data. This is probably due to the photon limit of *Chandra* data at the iron line energy band 6–7 keV. We thus re-estimated the mass of iron contained within a radius of $1\farcm5$ ($\simeq 20$ kpc) from the blob center. As we already mentioned in § 3.2.2, the projected iron abundance measured with *XMM-Newton* is $0.65 \pm 0.06 Z_\odot$, which is consistent with the *Chandra* value of $0.74^{+0.29}_{-0.23} Z_\odot$. After the deprojection as we did for the *Chandra* data (Hayakawa et al. 2004), the total mass of iron in the blob is estimated to be 1.9×10^7 $M_\odot$, which now becomes larger roughly by an order of magnitude.

The stellar mass of NGC 3311 is estimated to be 4.8×10^{11} $M_\odot$ from the relation $M/L_B = 8.5(M_\odot/L_\odot)$ with $m_B = 11.15$ (Faber et al. 1989). Assuming that the average iron abundance in the stellar mass of NGC 3311 is $1 Z_\odot$, we obtain the total stellar iron mass as $\sim 1.3 \times 10^9$ $M_\odot$. As a result, the iron mass of the northeast blob is $\sim 1.5\%$ of the stellar iron content, and

can reasonably be supplied by the single galaxy NGC 3311. Schindler et al. (2005) simulated metallicity evolution in galaxy clusters which includes interaction between the galaxies and the ICM. They have noted that the ram-pressure stripping is more efficient than the galactic wind in transferring metal-enriched interstellar medium into the ICM, and the expelled metals are not mixed immediately with the ICM. The northeast high-metallicity region, likely to be associated with NGC 3311, is reminiscent of the ram-pressure stripping from the X-ray image. If this is the case, NGC 3311 is moving with a velocity larger than a few 100 km^{-1} s in the central region of A 1060. The ram-pressure stripping is also likely to be the reason why this central galaxy shows a very compact X-ray halo (Yamasaki et al. 2002).

4.3. Temperature Distribution

Plasma temperature of the A 1060 cluster decreases from the center to $r = 13'$ by $\sim$30 %, which is a larger decrement than that detected in our *Chandra* observation ($\sim$20 %). This is probably because background uncertainty of the *Chandra* observation in the outer $r \gtrsim 10'$ region. Our result is consistent with that of Tamura et al. (2000) claiming that the temperature decreases down to about 2.4 keV at a radius of $\sim 12'-20'$ based on their analysis of the *ASCA* and *ROSAT* data.

Markevitch et al. (1998) observed 30 nearby clusters and obtained remarkably similar trend of the temperature normalized by the emission weighted average temperature $\langle T \rangle$, as a function of the radius normalized by r_{180}. We thus have attempted to plot our temperature profile with $r_{180} = 1.35$ Mpc (§ 4.1) and $\langle T \rangle = 3.3$ keV (§ 2). The resulting temperature profile is shown by diamonds in Fig. 7, while the composite profile of Markevitch et al. (1998) is shown as the region surrounded by the dashed line. The profile of A 1060 obviously becomes out of the allowed range in the region $r/r_{180} \gtrsim 0.07$. One possible reason to cause such a deviation may be an extra heating in the central region, due to a sub-cluster merger, for example. If we are allowed to take $\langle T \rangle = 2.5$ keV, for example, the normalized temperature profile well fits in the Markevitch's range, as displayed in Fig. 7.

We also recognize that there is a high temperature region at $r \simeq 7'$ from NGC 3311 in the southeast direction (Fig. 4). This feature can be confirmed also by the color-coded temperature map based on the HR analysis in Furusho et al. (2001). Figure 8 shows the radial surface brightness profile of the southeast direction, compared with that in the northwest direction in the top panel. The ratio of the two profiles (middle panel), and the radial temperature profile in the southeast direction (bottom panel) are also shown. The surface brightness around the position of the southeast hotter region is slightly fainter than that in the northwest region. The pressure P and the emissivity I are represented by the electron density n_{e} and the temperature T as $P \propto n_e T$ and $I \propto n_e^2 T^{1/2}$. Combining these relations by eliminating n_{e}, we obtain $P \propto I^{1/2} T^{3/4}$. At the southeast high temperature region, the surface brightness is lower than the northwest by $\sim 25\%$, while the temperature exceeds the linearly-fitted value by $\sim 20\%$. Thus, the southeast

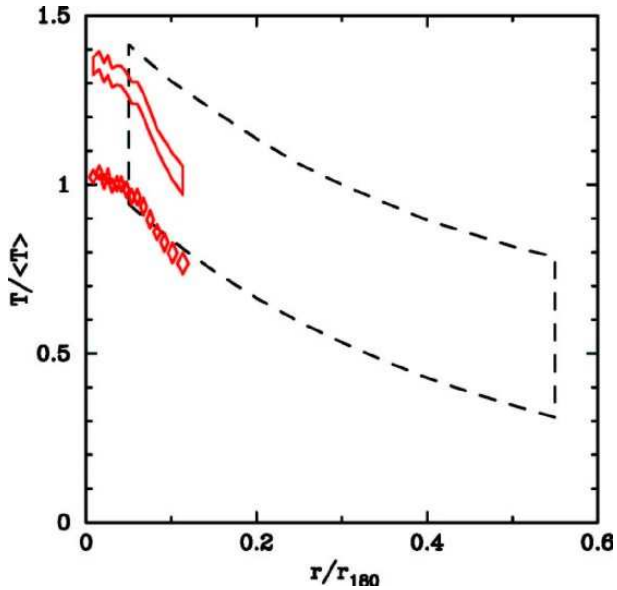

Fig. 7. Temperature distribution as a function of the radius from the cluster center in a unit of r_{180}. The diamonds and solid line correspond to the red diamonds in Fig. 3, normalized by the emission-weighted average temperature $< T >$ of 3.3 keV and 2.5 keV, respectively. The dashed line define a region that encloses most temperature profile and their error bars of Markevitch et al. (1998).

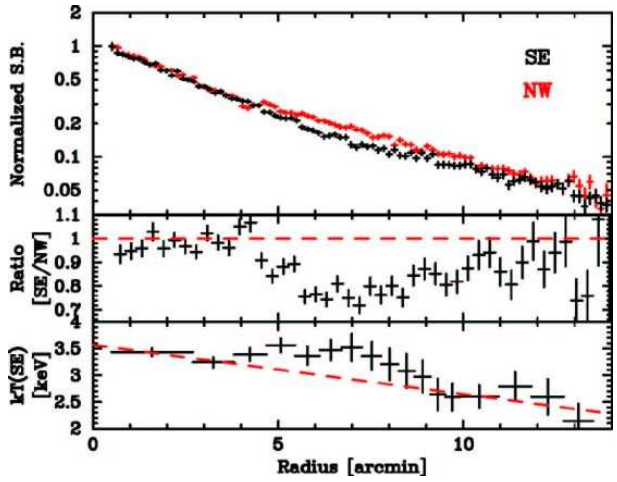

Fig. 8. Radial surface brightness profile in the SouthEast direction in comparison with the NorthWest (NW:red) (top), the ratio of these two profiles (middle), and the temperature distribution in SE direction (bottom). The dashed line in the bottom panel is the linear fit to the data in the range $r < 3'$ and $r > 10'$.

region is in pressure equilibrium with the environment. The diffusion time of pressure gradient is of the same order as the sound-crossing time. The time for reaching pressure equilibrium over the scale $3'$ ($\simeq 70$ kpc) can be estimated to be about 4×10^7 yr, for the sound speed of ~ 1000 km s^{-1}. On the other hand, the temperature difference of 1 keV over $3'$ distance is relaxed by thermal conduction whose time scale is estimated to be about 3×10^8 yr in the case of A 1060. It is likely that the temperature structure has been produced between 3×10^8 yr and 4×10^7 yr in the past.

5. Conclusion

We have presented the *XMM-Newton* observation of the A 1060 cluster of galaxies. Large effective area of *XMM-Newton* enables us to investigate spatial distribution of the surface brightness, the temperature and the metal abundance in unprecedented detail. We have derived a gravitational mass profile based on a model-independent estimation of the density profile. The overall shape can be well represented by Moore's profile with a central density slope $\propto r^{-1.5}$. The temperature is found to decrease undoubtedly by 30 % from the center to the edge of the field of view $r = 13'$. This drop is clearly steeper than the Markevitch's composite profile.

Our spatially-resolved analysis revealed slight temperature enhancement at $r \simeq 7'$ from NGC 3311 in the southeast direction. It is thought that some heating, like a subcluster merger, has occurred in this region in the past between the sound crossing time 4×10^7 yr and the thermal conduction time 3×10^8 yr ago. We note that the deviation of temperature profile of A 1060 from the Markevitch's one can also be explained if the central region is heated like the way seen in the southeast region.

The high resolution metallicity map for the central $r < 5'$ region confirmed the high-metallicity blob discovered with the *Chandra* observation locating at around $1'.5$ northeast of NGC 3311. Its spatial extent is, however, found to be as large as $r \sim 2'$, which is significantly larger than that estimated with *Chandra* ($r \sim 40''$). This discrepancy is probably because the *Chandra* observation is photon-limited in the iron line band. The iron mass in this region is revised to be 1.9×10^7 M$_\odot$. Although this is larger than the *Chandra* value roughly by an order of magnitude, it can still be supplied solely by NGC 3311.

References

Anders, E., & Grevesse, N. 1989, Geochim. Cosmochim. Acta, 53, 197

Churazov, E., Forman, W., Jones, C., Böhringer, H. 2003, ApJ, 590, 225

De Grandi, S., Ettori, S., Longhetti, M., & Molendi, S. 2004, A&A, 419, 7

Dickey, J. M., & Lockman, F. J. 1990, ARA&A, 28, 215

Durret, F., Slezak, E., Lieu, R., Dos Santos, S., & Bonamente, M. 2002, A&A, 390, 397

Durret, F., Lima Neto, G. B., & Forman, W. 2005, A&A, 432, 809

Evrard, A. E., Metzler, C. A., & Navarro, J. F. 1996, ApJ, 469, 494
Ezawa, H., Fukazawa, Y., Makishima, K., Ohashi, T., Takahara, F., Xu, H., & Yamasaki, N. Y. 1997, ApJL, 490, L33
Faber, S. M., Wegner, G., Burstein, D., Davies, R. L., Dressler, A., Lynden-Bell, D., & Terlevich, R. J. 1989, ApJS, 69, 763
Furusho, T., Yamasaki, N. Y., Ohashi, T. S. R., Kagei, T., Ishisaki, Y., Kikuchi, K., Ezawa, H., & Ikebe, Y. 2001, PASJ, 53, 421
Furusho, T., Yamasaki, N. Y., & Ohashi, T. 2003, ApJ, 596, 181
Hayakawa, A., Furusho, T., Yamasaki, N. Y., Ishida, M., & Ohashi, T. 2004, PASJ, 56, 743
Katayama, H., Takahashi, I., Ikebe, Y., Matsushita, K., & Freyberg, M. J. 2004, A&A, 414, 767
Markevitch, M., Forman, W. R., Sarazin, C. L., & Vikhlinin, A. 1998, ApJ, 503, 77
Markevitch, M., et al. 2000, ApJ, 541, 542
Mazzotta, P., Edge, A. C., & Markevitch, M. 2003, ApJ, 596, 190
Moore, B., Quinn, T., Governato, F., Stadel, J., & Lake, G. 1999, MNRAS, 310, 1147
Navarro, J. F., Frenk, C. S., & White, S. D. M. 1996, ApJ, 462, 563
Navarro, J. F., Frenk, C. S., & White, S. D. M. 1997, ApJ, 490, 493
Piffaretti, R., Jetzer, P., Kaastra, J. S., & Tamura, T. 2005, A&A, 433, 101
Pratt, G. W., & Arnaud, M. 2002, A&A, 394, 375
Read, A. M., & Ponman, T. J. 2003, A&A, 409, 395
Schindler, S., et al. 2005, A&A, 435, L25
Tamura, T., et al. 1996, PASJ, 48, 671
Tamura, T., Makishima, K., Fukazawa, Y., Ikebe, Y., & Xu, H. 2000, ApJ, 535, 602
Yamasaki, N. Y., Ohashi, T., & Furusho, T. 2002, ApJ, 578, 833